Effect of carbon nanofiber surface morphology on convective heat transfer from cylindrical surface: Synthesis, characterization and heat transfer measurement

T.J. Taha [a], *, B.L. Mojet [b], L. Lefferts [b], T.H. van der Meer [a]

[a] Thermal Engineering, Faculty of Engineering and Technology, University of Twente, 7500 AE, Enschede, Netherlands
[b] Catalytic Processes and Materials, Faculty of Science and Technology, University of Twente, 7500 AE, Enschede, Netherlands

ABSTRACT

In this work, heat transfer surface modification is made by layers of carbon nanofiber (CNF) on a 50 μm nickel wire using Thermal chemical vapor deposition process (TCVD). Three different CNF layer morphologies are made, at 500 °C, 600 °C and 700 °C, to investigate the influence of morphology on heat transfer performance characteristics. Experimental results show that a CNF layer made at 500 °C behaves like an additional heat resistance, which is attributed to the dense structure of the layer of fibers. This results in 25% lower heat transfer compared to the heat transfer performance of the bare wire. However, samples made at 600 °C, exhibit a relatively porous layer of CNFs with relatively lower thermal conductivity compared to samples made 500 °C, resulting in an enhancement of 24%. This is because the relative porous structure leads to relatively better flow permeability which reduces the thermal resistance of the layer. Samples made at 700 °C are partly covered with a dense CNFs layer and partly with an amorphous layer of carbon. Heat transfer enhancement of 34% is achieved which is attributed to the combined effect of the highly conductive layer, high effective heat transfer surface area and rough surface morphology.

© 2016 Elsevier Masson SAS. All rights reserved.

1. Introduction

Advancements of current heat transfer technologies are triggered by energy, material and economic considerations, which contribute to more sustainable, efficient and cost effective systems. Both passive [1—6] and active [7—10] methods of enhancing heat transfer have been the focus of many studies in the heat transfer research community. The classical approach of enhancing heat transfer equipment is by modifying the heat transfer surface, which leads to maximizing the surface area and better hydrodynamic boundary layers.

Heat transfer surface modification — on micro-scale — plays a significant role on the current technological advancements where space, mass and power density are important. The remarkable discovery of the CNTs [11] — with extremely high thermal conductivity and mechanical properties - paved the way to harness the novel properties in many industrial applications. This novel material is a potential candidate for application areas such as electronic chips, catalyst support materials, micro-electro-mechanical systems (MEMS), evaporator walls (cryogenic refrigeration), regenerators (stirling engines, thermo-acoustic heat pumps, thermo-chemical heat pumps), where heat removal is a critical design parameter. Due to their extremely high thermal conductivity, attributed to the strength of the carbon—carbon bond within graphene layers, carbon nanotubes are considered as a novel material in heat transfer research [12—15]. This new material however has a highly anisotropic thermal conductivity. The thermal conductivity at room temperature along the a-axis (in-plane) of the graphene layer is greater than 3000 W/m K [16] while the conductivity along the c-axis (out of plane) can be as poor as 1.52 W/m K [17]. As a result, the structural arrangement of graphene layers has a tremendous influence on the thermal properties. Carbon nanostructures exist in three different graphene layer arrangements: perfect cylindrical arrangement of graphene sheets (Tubes), conical arrangement of the graphene sheet (fish-bone) and flat graphene arrangement (stacked). Fig. 1 shows the structural arrangement of the graphene layer on the CNFs produced. The black lines signify the graphene layer (one-atom thick layer)

* Corresponding author.
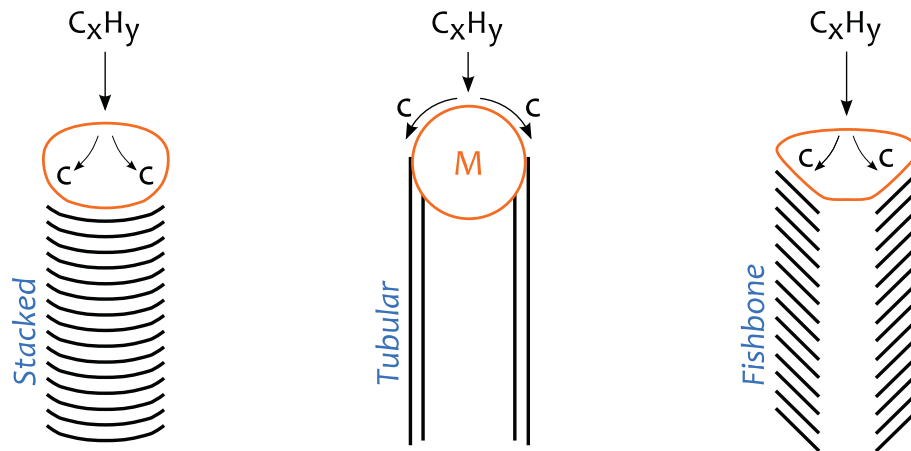 *E-mail addresses:* t.j.taha@utwente.nl, t_1915@yahoo.com (T.J. Taha).

Fig. 1. Schematic illustration of the different forms of Carbon nanofibers with different graphene layer arrangement, where the black lines represent the graphene layer arrangement.

arrangement. These different structures are believed to have different effective thermal conductivities. Moreover, the thermal conductivity of carbon nanostructures is strongly dependent on the degree of crystallinity, crystallite shape, crystallite size, and presence of impurities. However, quantitative measurement of thermal transport properties of individual fibers remains challenging, due to technological difficulties associated with nano-scale experimental measurements [18].

Preliminary experimental research has shown that carbon-nano-fibers deposition may lead to both increase and decrease in heat transfer performance. Tuzovskaya et al. [19] performed experimental investigations on stainless steel and on carbon foam. CNF's on stainless steel resulted in enhancement of heat transfer ranging from 30% to 75%, while CNF's on carbon foam decrease heat transfer by 40%. It was explained that the cumulative effect of an increase of heat exchange surface area, the structural arrangement of the graphene layer and the higher crystallinity results in the overall performance of the stainless steel foam.

Kordas et al. [20] have reported an efficient chip cooling by integrating both laser patterned CNT and copper micro fin structures on a silicon chip. It was reported that micro-fin chip dissipates more power (up to ~1 W from 1mm2 surface) compared to a bare chip. Similar enhancement results were reported for both CNTs and copper structures for both natural and forced convection with an enhancement of 11% and 19% respectively. However, an un-patterned CNTs layer shows poor heat transfer performance due to the dense nature of the CNTs layer hampering the flow of N_2 in the film, limiting the heat transfer only to the upper facet of the films, resulting in limited cooling capabilities. It is also suggested that by changing fin geometry, dimension and fin densities more efficient cooling can be achieved.

Zhimin Mo et al. [21] reported effective cooling for microelectronic applications using integrated CNT fins made by lithographic technique and CVD on a micro-channel surface. It was mentioned that the flow rates were decreased by 12% whereas the heating power input is increased by 23% keeping the transistor temperature 6 °C below the reference cooler. It was also suggested that self-aligned CNTs would increase the heat transfer even more than what was achieved.

The aim of the present work is to explore the influence of the morphology of carbon-nanostructured surfaces on heat transfer performance characteristic. The heat transfer performance test was made on a 50 μm diameter nickel wire by modifying the surface with a layer of carbon nanofibers-(CNFs) with varying surface morphology.

2. Materials

Polycrystalline Ni wire (99.9%, Ni270, Alloy Wire International Ltd.), made by a wire drawing mechanism, with a uniform diameter of 50 μm was used in this study to represent a differential strand of common regenerator element such as metallic foam, see Fig. 2. The surface of the wire was modified by depositing carbon nano-structural layer. High purity gases were used during the synthesis process: hydrogen (99.999%, INDUGAS), nitrogen (99.999% INDU-GAS) and ethylene (99.95% PRAXAIR).

3. Experiment

3.1. CNFs layer synthesis

Three different sample synthesis procedures were used to obtain different CNFs topological structures. Prior to CNF-synthesis, the Nickel micro wire samples were pretreated under a reducing atmosphere in a 50 mm diameter vertical quartz reactor which was heated from outside by an electrical furnace. The samples were heated to 600 °C with a heating rate of 6 °C/min under a nitrogen (inert medium) stream with a total flow rate of 100 ml/min. After reaching 600 °C, 30 vol.% hydrogen was introduced in the nitrogen stream to reduce the samples for 1 h, while maintaining the total flow rate at 100 ml/min. It should be noted that all samples undergo the same pretreatment in order to have a relatively equal number of nucleation sites, which helps to determine the influence of the synthesis temperature on the morphology of the synthesized nano-fibers. After the reduction pretreatment, the samples were brought to the synthesis temperature (500 °C, 600 °C and 700 °C) at a rate of 6 °C/min under a nitrogen stream with a total flow rate of 100 ml/min. The samples were further exposed to a reactive gas mixture of 20 vol.% C_2H_4, 5 vol.% H_2 and 75 vol.% N_2 at 500 °C, 600 °C and 700 °C with total flow rate of 100 ml/min. Subsequently, the samples were cooled down in N_2 to room temperature. Finally, samples were further exposed to a jet of air in order to remove any loosely attached carbon nanofibers. The samples synthesized at 500 °C, 600 °C and 700 °C with respect to the synthesis duration will be referred throughout the paper as "CNF5-[n]", "CNF6-[n]" and "CNF7-[n]" respectively, where n stands for the synthesis duration.

3.2. Characterization of CNFs layer

The morphology of the samples was studied with high resolution Scanning Electron microscopy (HR-SEM-LEO-1550)
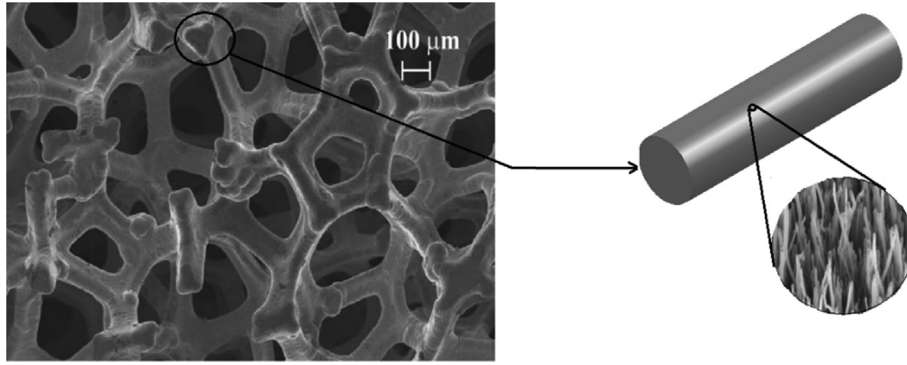
Fig. 2. A 50 μm cylindrical wire representing a metallic foam regenerator strand for heat transfer surface modification process.

equipped with NORAN EDS and WDS. The average layer thickness of the CNFs layer and the CNFs diameter was estimated based on 25 observations of SEM images post-processed in MATLAB. Prior to the layer thickness measurement, samples were frozen in liquid nitrogen and a cross-sectional cut is achieved using a scalpel. Raman analysis was performed using a Senterra Raman spectrometer (Bruker Optik GmbH) to probe the crystallinity of the CNF layer, which helps to determine the alignment of the graphene planes. The graphene plane arrangement influences the conductivity of the CNFs produced by analyzing the defects. The spectrometer was equipped with a CCD detector cooled at 208 K (-65 °C). Raman scattering was conducted in the backscattering configuration with a green laser (wavelength = 532 nm) at room temperature. The Raman spectrometer was equipped with an optical microscope, which was used to focus the incident laser and record the illuminated area. The spectral resolution was ~9–15 cm^{-1} and the optical power at the sample was maintained at 5 mW. Spectra were recorded for an integration time of two seconds and averaged over ten scans to improve the signal-to-noise ratio. The sample was analyzed without any sample treatment or preparation.

3.3. Heat transfer measurement setup

A schematic diagram of the heat transfer setup is shown in Fig. 3. Air was supplied from a 6 bar air supply and the flow was controlled by a mass flow controller. The air passes through a flow straightener and reaches the nozzle. The nozzle was designed to achieve a constant velocity profile at the exit. A mass flow controller is used to determine the flow speed from the nozzle (U_∞) through the nozzle cross-section. Sample wires were spot welded onto a probe and placed perpendicularly facing the flow. The probe was electrically heated to a desired temperature and the temperature of the air flow (T_∞) was measured. An electric current (I) was supplied and regulated by a high precision DC power supply (Tektronix PWS4205). The amount of voltage drop and the resistance (R_w) were measured using a NI-PCI-6280 module. The fluid properties such as conductivity (k_f), viscosity (μ_f) and density (ρ_f) are evaluated at film temperature. The sample is made up of high purity (99.9%Ni) polycrystalline nickel micro wire (Ni270) which is also used as a catalyst and substrate material during the synthesis of the CNF layer. Heat transfer measurements of the bare micro wire (d) were compared with different correlations from literature and satisfactory results were obtained [23]. The Nusselt (Nu_d) and Reynolds (Re_d) numbers are calculated as:

$$Nu_d = \frac{I^2 \cdot R_w}{k_f \cdot \pi \cdot l \cdot (T_w - T_\infty)} \tag{1}$$

$$Re_d = \frac{\rho_f \cdot U_\infty \cdot d}{\mu_f} \tag{2}$$

The heat transfer performance of the modified wire surfaces are compared and heat transfer enhancement is computed as:

$$\eta = \left[\frac{Nu_{d(CNF)}}{Nu_{d(bare)}} - 1 \right] \cdot 100\% \tag{3}$$

Based on the work of Moffat et al. [24], measurement uncertainties are analyzed. Based on 120 data samples, results show that the uncertainty of the measured Nusselt number is $\pm4.4\%$.

The porosity and permeability are important parameters to anticipate the amount of flow penetration inside the CNF layer. Due to the curvature effect of the CNFs covered samples, the porosity and flow permeability increase in the radial direction. This creates a region inside CNFs sub-layer with the highest flow restriction in the inner region of the layer. As a result, it is difficult to determine the effective diameter of individual samples made. Hence, it affects the heat transfer comparison of each different sample with respect to the flow characteristics.

4. Results and discussion

4.1. CNFs layer synthesis

CNFs synthesis was successfully achieved on a 50 μm nickel wire with three different synthesis temperatures (500 °C, 600 °C and 700 °C). The surface morphology proved to be highly dependent on the synthesis temperature [25]. The thickness of the layer varies mainly with the synthesis duration and temperature. Different surface morphologies are attained when carbon deposition temperature varies from 500 °C to 700 °C, see Fig. 4. The porosity and the permeability of the CNF layers are expected to increase along the radial direction. This is due to the curvature effect of the 50 μm nickel substrate which hardly leaves any voids close to the polycrystalline nickel surface and larger voids on the outer most surface. In addition, tip growth of the CNFs is observed at all three synthesis conditions.

To study the structural difference created by changing the synthesis temperature, samples (CNF5-60, CNF6-60 and CNF7-30) were analyzed using SEM see Fig. 4. The CNFs layer thickness was on average 55 μm, 59 μm and 19 μm for growth temperature of 500 °C, 600 °C and 700 °C respectively, see Table 1. In addition to
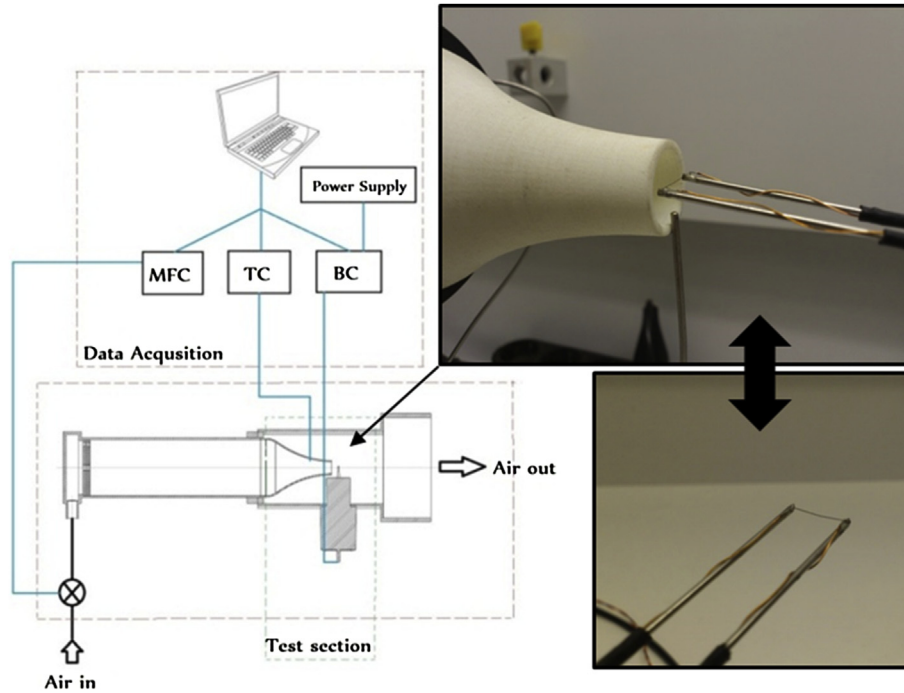
Fig. 3. Schematic view of heat transfer measurement setup adopted from Ref. [22].

the thickness of the layers of CNFs, the range of diameters of the individual fibers appeared to be different for the three samples. The average diameter of the fibers increased with synthesis temperature. SEM images show that the CNF5-60 sample is made up of large strands of fibers (~120 nm) entangled with small fibers (as small as 8 nm), which increases the density of the fibers population, hence resulting in a denser layer. Sample CNF6-60 shows a relatively porous CNF morphology, compared to the CNF5-60, with fiber diameters ranging from 30 nm to 120 nm, see Fig. 4a and b. Sample CNF5-60 and CNF6-60 are entirely covered with a CNFs layer while CNF7-30 is partly covered with fibers and partly with a carbon layer (Fig. 4c).

4.2. Analytical comparison of CNFs layer flow permeability

Meso- and micro scale porous materials were given a particular attention for their extremely high surface area for both as a substrate material for catalyst support [26–28] and heat transfer application [19,29,30]. However, it is a challenge to thoroughly investigate both the fluid flow and heat transfer characteristics of micro-porous media. The flow and heat transfer behavior within the porous layer of CNFs can be characterized by the characteristic size and structural complexity of the fibers network. The level porosity of the CNFs layer insures the physical contact between the fluid and the fiber network which directly influences both the flow and heat transport. In addition to the level of porosity, the flow permeability is an important parameter which measures the ability of the porous material to convey fluid through the porous media. Fluid flow inside a porous material can be estimated based on Darcy flow law [31] as follows:

$$u = -\frac{\kappa}{\mu} \cdot \frac{\Delta P}{L} \qquad (4)$$

where u is the average fluid velocity [m/s], μ [Kg/ms] dynamic viscosity, L [m] characteristic length, ΔP [Pa] is the pressure drop, κ

[m^2] is fluid permeability of the porous media. The flow permeability depends on both porosity and diameter of the fibers. Ergun [32] studied flow through a porous medium by considering the internal structure. He derived a semi-empirical expression, which relates the porosity (ϕ [−]) and the characteristic size (d [m]) to the permeability. The fluid permeability (κ [m^2]) is described as:

$$\kappa = \frac{1}{c} \cdot \frac{\phi^3}{(1-\phi)^2} \cdot d^2 \qquad (5)$$

where c [-] is an empirical constant dependent on the shape and size of the porous material. From Equation (5), it can be seen that for samples with a specific porosity, the flow permeability is proportional to the square of the fiber diameter ($\kappa{\sim}d^2$). For a specific fiber diameter and low porosity of the CNF layer, the permeability is proportional to ϕ^3. While for high porosity, the permeability is proportional to $1/(1-\phi)^2$. Fachin et al. [33] tested the permeability of vertically aligned carbon nanotube (VACNT) pillars, with fiber diameter of 8 nm and pore size of 80 nm. The experimental values of the permeability obtained during their study have a good comparison with the one obtained using Equation (5), where c = 150 (as per Ergun's original work). Lysenko et al. [34] experimentally determined the gas permeability of porous silicon nanostructures, with 16 nm diameter and 7 nm pore size. Similarly, the permeability results obtained shows a good agreement with Ergun's semi-empirical correlation. As a result, Ergun's correlation is used as a tool to compare the flow permeability of CNFs samples based on the fiber diameter and porosity.

The amount of carbon deposited on sample CNF5-60 is 85% higher than the amount deposited on sample CNF6-60 while the layer thickness of sample CNF5-60 is 7% smaller than sample CNF6-60. This indicates that sample CNF5-60 has a lower porosity than sample CNF6-60. Using the semi-empirical relation of Ergun (Equation. (5)), the permeability of CNF5-60 and CNF6-60 are calculated to be 1.9e-16 [m^2] and 8.6e-15[m^2] respectively. This supports the previous argument made from the SEM image
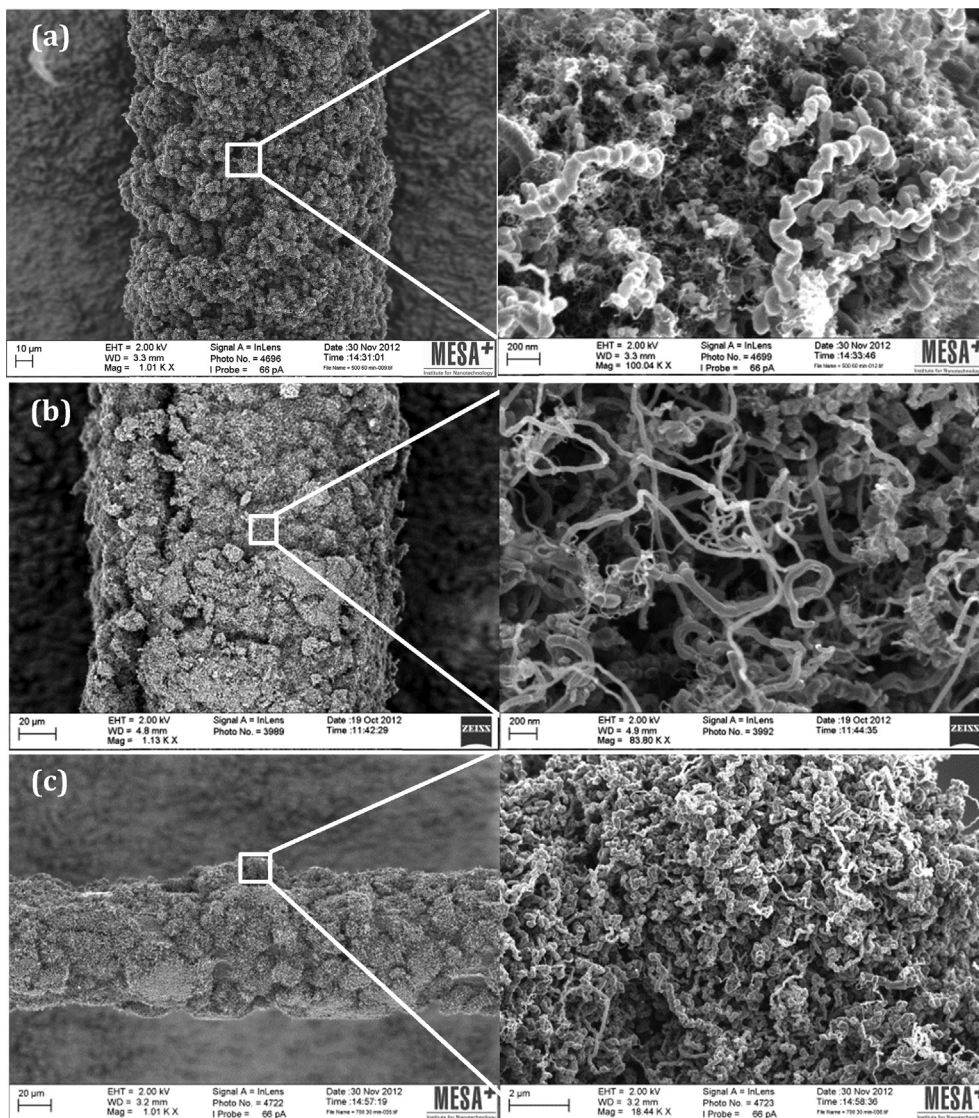
Fig. 4. SEM images of the surface morphology of a CNFs layer produced on 50 μm Nickel wire. (a) densely populated CNFs layer grown at 500 °C for 1hr which is made up of smaller fibers as small as 8 nm diameter entangling larger ones (~100 nm), (b) CNFs layer produced at 600 °C for 1hr with a relatively porous CNFs layer, and (c) CNFs layer grown at 700 °C for 30 min have rougher morphology and porous CNFs structures as well.

Table 1
Carbon nanofibers structural characteristics.

CNFs samples	Layer thickness [μm]	Fiber-diameter -range (avg.) [nm]	Carbon deposit [g_C/g_{Ni}]	Porosity[a] ϕ [−]	Permeability[b] κ [m²]
CNF5-60	~55	8−120 (20)	~0.237	0.899	1.9e-16
CNF6-60	~59	30−120 (60)	~0.128	0.951	8.6e-15
CNF7-30	~19	80−200 (120)	~0.302	−	−

[a] Assuming the density of individual CNFs to be equal to that of graphite, the porosities are calculated using the carbon mass deposit data and CNFs layer thickness information. However, since CNF7-30 is significantly covered with thick C-layer, only a comparison is made for the CNF7-30 with respect of the rest of the samples.
[b] The permeability value measured is the average value along the layer thickness.

observation. However, sample CNF7-30 shows to have an entirely different CNFs layer morphology compared to samples CNF5-60 and CNF6-60. Sample CNF7-30 has a larger fiber diameter, as large as 200 nm, and a relatively large amount of carbon deposit per CNFs layer thickness, see Table 1. As result, it is difficult to determine the permeability of CNFs samples grown at 700 °C and comparing their flow penetration through CNFs layers, because a significant portion of the deposition area is covered by a C-layer.

4.3. Analytical thermal conductivity comparison using Raman spectra

Similar to other non-metallic materials, the transport of thermal energy in carbon nanofibers or tubes is assumed to occur via the phonon conduction mechanism. Phonon conduction in these structures is influenced by several processes such as the number of phonon active modes, the boundary surface scattering, the length

of the free path of the phonons and inelastic Umklaap-scattering (an anharmonic phonon–phonon or electron phonon scattering process) [35,36]. The thermal conductivity of the carbon nanostructures is dependent on how the graphene layers are arranged, the diameter and the length of the filaments, the number of structural defects and morphology, and on the presence of impurities [37,38].

Graphene layers have highly anisotropic physical properties which influences the physical properties of individual fibers. For instance, the in-plane thermal conductivity of the graphene layer is 2–3 orders of magnitude greater than the conductivity along the c-axis. As a result, the effective thermal conductivity of individual fiber, which consists of both in-plane and out of plane, is strongly dependent on the quality of the crystallite [39,40]. As a result, the factors influencing the in-plane thermal conductivity also determine the overall conductivity of the individual of graphitic material. However, the effective thermal conductivity of a bundle of CNFs depends not only on the thermal properties of the individual nanofibers, but also on the porosity, the graphene layer alignment and the flow permeability of the layer. As a result, the thermal conductivity measurement of CNFs layers creates large uncertainty. However, it is possible to systematically compare the quality of a graphitic layer of each sample by using Raman spectral data.

Raman spectroscopy is widely used as a tool to characterize graphitic materials such as pyrolytic graphite, carbon fibers, carbon nano fibers and carbon nano tubes. These materials have a distinct structural difference of the graphene layer arrangement. The basic structural properties of these graphene based materials, such as the in-plane crystallite size [41,42] and out-of-plane stacking order [42–44], strongly affect their corresponding Raman spectra. In this section, the CNFs that are produced under different experimental conditions will be compared on their thermal conductivity using Raman spectra results. The comparison mainly focuses on the quality of the graphene layers of the individual carbon nanofibers.

The crystallinity of the CNFs layer has a great influence on the thermal conductivity of the material due to the graphene layer arrangement [16,17]. The Raman spectra of CNF layer synthesized on Ni wire is featured D and G bands which is typical for carbon nanostructures, see Fig. 5. Two clear bands are visible for all samples, centered between ~1335 and ~1586 cm^{-1}. It is known that the Raman spectrum of single-crystal graphite, as well as of highly oriented pyrolytic graphite (HOPG) have a single band at ~1582 cm^{-1} (G-band), which is known as the graphite mode. Carbon materials with less order of crystallinity exhibit a band at ~1350 cm^{-1}, which is a defect induced Raman band which is associated with the sp^3 mode named as the defect mode (D-band) [45,46]. The ratio of the relative integrated intensity of the D-band and G-band (I_D/I_G) can be utilized to assess the degree of graphitization and the alignment of the graphene planes.
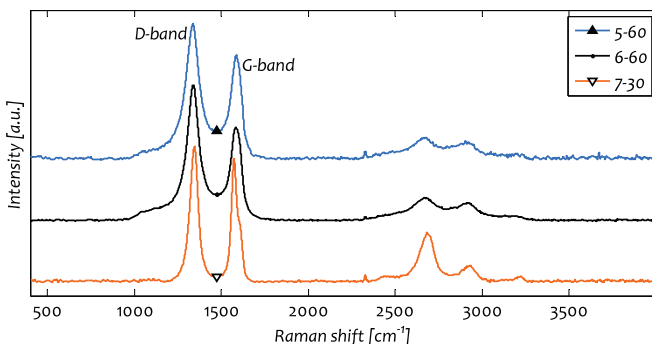
It is important to note that CNF7-30 is made up of a CNFs layer and a separate carbon layer, see Fig. 4c. In order to have a fair comparison of the CNFs layers for the different samples, the Raman spectra measurement of sample CNF7-30 was done by focusing the laser beam on the CNFs layer. Sample CNF5-60 and CNF6-60 have almost the same position of D-band and G-band, see Table 2. In addition, the intensity ratio difference, among the two samples, is relatively small when it is compared to CNF7-30. The structural disorder of the graphene layer reveals itself as a varying (I_D/I_G) intensity ratio, which is proven physically to be related to crystallite size of well-ordered graphene (L_a). In another words, the smaller the relative intensity ratio of the carbon nanostructures, the more ordered (less defect) and more crystalline the layer of carbon nanostructures [47,48]. Cançado, L.G., et al. [49] experimentally obtained a ratio between the integrated intensities (I_D/I_G) of the disorder-induced D and G Raman bands in nano-graphite samples with different crystallite size (L_a) using different excitation laser energies. The general expression obtained to estimate the crystallite size using any laser line in visible range is:

$$L_a \ [nm] = \frac{560}{E_l^4} \cdot \left(\frac{I_D}{I_G}\right)^{-1} \tag{6}$$

where E_l is the laser excitation energy used in the Raman experiment in eV units. Equation (5) can also be expressed as a function of the wave length (λ_l) in nanometer:

$$L_a \ [nm] = \left(2.4 \times 10^{-10}\right) \cdot \lambda_l^4 \cdot \left(\frac{I_D}{I_G}\right)^{-1} \tag{7}$$

Using Equation (7), the calculated crystallite size for CNF5-60, CNF6-60 and CNF7-30 is 13 nm, 12 nm and 17 nm respectively. Theoretical estimates of the thermal conductivity of a single crystals of graphite, as done by Klemens et al. [38], can be used as a tool to compare the phonon thermal conductivity in the a-plane at room and at elevated temperature. The thermal conductivity in graphitic materials in the presence of grain boundary scattering is derived by integrating the phonon spectrum changed as a result of the grains that creates a size dependent cut-off frequency ω_G. The thermal conductivity in the presence of grain boundary scattering is obtained by:

$$K = K_0 \frac{1}{2} \frac{ln\left(\frac{\omega_m^2 + \omega_G^2}{\omega_c^2 + \omega_G^2}\right)}{ln\left(\frac{\omega_m}{\omega_c}\right)} \tag{8}$$

where K_0 is the defect free thermal conductivity of graphene layer, the maximum cut-off phonon frequency $\omega_m = 2.88 \times 10^{14} [s^{-1}]$ and the low bound cut-off phonon frequency of $\omega_c = 2.5 \times 10^{13} [s^{-1}]$. Using these frequencies, Klemens et al. [39] calculated the in-plane thermal conductivity to be 1910 W/m K at 300 K, which is in reasonable agreement with highly ordered pyrolytic graphite (HOPG) ranging from 1660 W/m K [50] to 1840 W/m K [51]. The resulting thermal conductivity of Klemen's approach shows the size dependence cut-off frequency to be $\omega_G = 5.8 \times 10^{12} \ T^{-0.5} L_a^{-0.5} [s^{-1}]$. This approach

Fig. 5. Raman spectra of CNFs with different synthesis conditions.

Table 2
Raman spectral data.

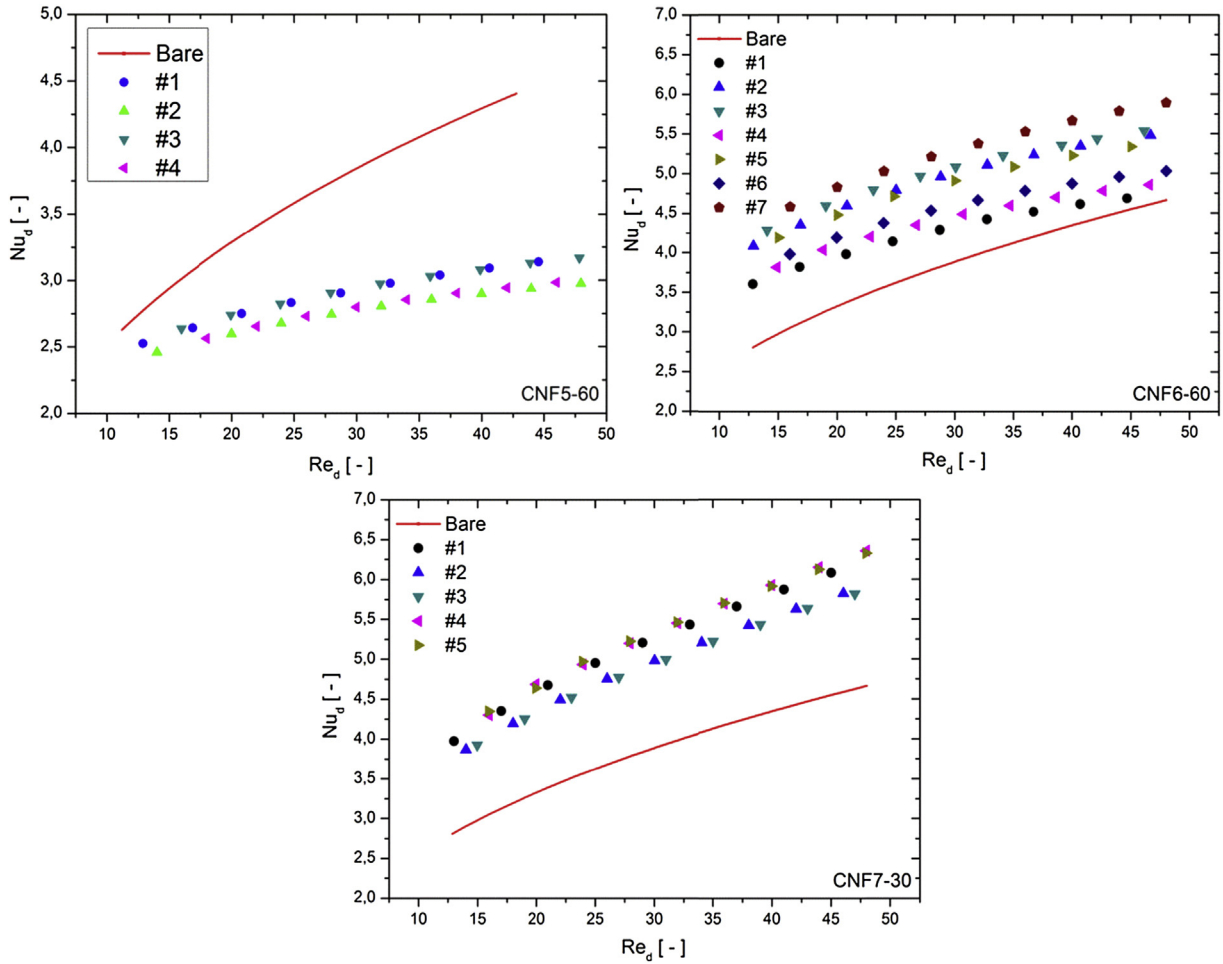| CNFs samples	D band [cm^{-1}]	G band [cm^{-1}]	I_D/I_G	L_a [nm]
CNF5-60	1335	1586	1.301	13
CNF6-60	1336	1583	1.457	12
CNF7-30	1345	1572	1.099	17

Fig. 6. Heat transfer characteristics of 50 μm wire covered with CNFs layer compared to bare wire.

helps in estimating the relative thermal conductivity ratio between the samples. The thermal conductivity, based on the presence grain boundary scattering, of CNF5-60 and CNF7-30 is ~13% and ~37% higher than CNF6-60 at 300 K. Similar dependency of thermal conductivity to L_a is derived by shortening the phonon mean free path by $(1 + \omega/\omega_0)$ to account for point defect in the graphitic material [39], which is given as:

$$K = K_0 \left(1 - \frac{ln\left(\frac{\omega_m + \omega_0}{\omega_c + \omega_0}\right)}{ln\left(\frac{\omega_m}{\omega_c}\right)} \right) \quad (9)$$

The characteristic scattering frequency can be calculated as $\omega_0 = 2.83 \times 10^{-7} \omega_m \frac{T}{c} [s^{-1}]$. Where T is temperature in K and c is the effective defect concentration. The defect concentration is inversely proportional to La ($c \sim L_a^{-1}$), resulting in a direct proportionality of ω_0 to L_a. Using Equation (9), assuming point defect concentration from 1% to 5%, the thermal conductivity CNF5-60 and CNF7-30 is 8%–12% and 41%–44% higher than CNF6-60 at 300 K.

4.4. Convective heat transfer

In the previous section, the different CNFs samples are compared for their flow penetration propensity and thermal conductivity. In this section, the three different CNFs samples, synthesized at 500 °C, 600 °C and 700 °C, are experimentally investigated for their convective heat transfer behavior with respect to their CNFs layer morphology. The heat transfer performance of each sample tested compared to the heat transfer performance of a bare wire can be seen in Fig. 6, where the original diameter of the bare wire is used as a characteristic diameter during the heat transfer analysis. To insure the reproducibility of the heat transfer measurements, a number of measurements were done for each case. This was done by repeating the heat transfer experiment several times using a new sample produced at the same synthesis temperature, see Fig. 6. The spread of results obtained during the measurement can be caused by both the mechanical stability of the layer deposited during the spot welding process and/or the local morphological difference that can be obtained from sample to sample.

It is well known that CNFs layer exhibit extremely high surface area which can be harnessed depending on the flows penetration through the layer [19,52]. The thermal conductivities of the graphene sheet of the representative samples were compared as CNF7-30 > CNF5-60 > CNF6-60, whereas the flow permeability was compared as CNF6-60 > CNF5-60. However, it was rather difficult to compare the permeability of the CNFs layer produced at 700 °C due to the morphological difference created by the accompanying C-layer. The heat transfer performance of CNF5-60 on average is 26% less than the bare wire. This result is attributed to the highly dense layer of CNF5-60, which prevents flow from penetrating in to the layer. As a result, the trapped air creates an insulating layer. In contrary, the dense layer CNF5-60 shows better mechanical

stability during the spot welding process. This can also be seen by the lower dependency of the Nusselt number to the flow compared to the CNF6-60. In contrary, CNF6-60 shows better performance compared to the bare wire with an average enhancement of 24%. These results are attributed to the permeable nature of the thermal conducting CNFs layer, which allows partial or full penetration of the flow facing the sample. The flow penetration inside CNFs layer results to either increasing the heat exchanging surface area, increasing the effective thermal conductivity inside the thermal boundary layer or both. Similar decreasing trend of the Nusselt number with the flow can be seen CNF6-60, this can be due to the flow separation which results less flow penetration; hence partially insulating the sample. However, the highly porous structure of samples produced at 600 °C resulted in weak mechanical stability compared to CNF5-60. This weak mechanical stability was witnessed during spot-welding the sample on the probe. As a result, CNF6-60 have wide scattering of data created due to the loss of layers of fibers during the spot-welding of the samples. Further investigation shows that after removing the layer of carbon nanostructures the bare wire results were reproduced again (results not shown here). An exceptional heat transfer enhancement of 34% is achieved by sample CNF7-30. Compared to the bare sample, similar increasing trend can be seen for this sample with respect to the flow. This means sample CNF7-30 have less insulation potential than the rest of the samples. This is highly attributed to its highly conductive CNFs layer with exceptionally rough surface morphology which influences the hydrodynamic boundary layer of the flow and increases the surface area of heat transfer as well.

The abrupt change of the CNFs layer porosity of the sample from inner most nickel surface (~0%) to the outer most CNFs surface (>99%) results in a significant change in flow permeability across the CNFs layer thickness. This makes it difficult to obtain the effective characteristic diameter (d_{eff}) on which the dimensionless number Re and Nu should be based upon. For this reason, the overall performance of the CNFs samples tested are evaluated for both the inner most diameter (d_i) and the outer most diameter (d_0) of individual samples. Results can be found in Fig. 7. The heat transfer enhancement obtained by assuming the inner and the outer diameter of CNF5-60 ranges from −26% to −53% respectively. As a result, no enhancement can be obtained from the samples produced at 500 °C. The enhancement of sample CNF6-60 ranges from 24% to −22% by using the inner and outer most diameters
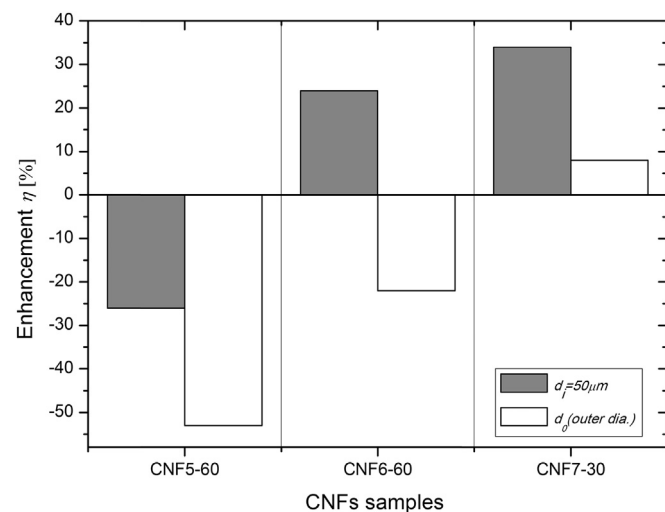
respectively. This result shows the importance of determining the effective diameter in order to obtain the accurate non-dimensional heat transfer property of the samples. On the other hand, better heat transfer performance is obtained for samples produced at 700 °C for their respective range of diameters. The average heat transfer enhancement of CNF7-30 was found to be 34%−8% respectively. However, it is technically difficult to quantitatively determine the effective diameter of each sample in order to quantify their respective dimensionless heat transfer behavior.

5. Conclusions

Using a TCVD process, successful synthesis of carbon nanofibers with different surface morphology on a 50 μm nickel was obtained. Both the influence of morphology and CNFs layer thickness are studied by evaluating the physical characteristics of the CNFs layer (thermal conductivity and flow permeability). Since the CNFs layer is a highly porous layer, the thermal conductivity of the layer depends on the individual property of the fibers and on how much flow can penetrate through the different layers of CNFs. Results from CNF5-60 has lower flow permeability compared to CNF6-60, but higher thermal conductivity of the individual layers. However, the effective thermal conductivity is lower than samples produced at 600 °C. This result in lower heat transfer performance of CNF5-60 compared to CNF6-60. CNF7-30 has an exceptional heat transfer performance, which is attributed to the combined effect of the high thermal conductivity of the layer, high effective heat transfer surface area and rough surface morphology of the samples.

Acknowledgment

Fig. 7. Overall performance evaluation of the CNFs samples with comparisons of characteristic diameter of the bare wire (50 μm) and outer most diameters of each samples.

References

[1] N. Khan, D. Pinjala, K.C. Toh, Pool Boiling Heat Transfer Enhancement by Surface Modification/Micro-Structures for Electronics Cooling: A Review, 2004, pp. 273–280, http://dx.doi.org/10.1109/EPTC.2004.1396618.

[2] A. Miyara, Y. Otsubo, S. Ohtsuka, Y. Mizuta, Effects of fin shape on condensation in Herringbone microfin tubes, Int. J. Refrig. 26 (4) (2003) 417–424, http://dx.doi.org/10.1016/S0140-7007(02)00154-8.

[3] L. Tadrist, M. Miscevic, O. Rahli, F. Topin, About the use of fibrous materials in compact heat exchangers, Exp. Therm. Fluid Sci. 28 (2–3) (2004) 193–199, http://dx.doi.org/10.1016/S0894-1777(03)00039-6.

[4] K. Boomsma, D. Poulikakos, F. Zwick, Metal foams as compact high performance heat exchangers, Mech. Mater. 35 (12) (2003) 1161–1176, http://dx.doi.org/10.1016/j.mechmat.2003.02.001.

[5] T.J. Lu, H.A. Stone, M.F. Ashby, Heat transfer in open-cell metal foams, Acta Mater. 46 (10) (1998) 3619–3635, http://dx.doi.org/10.1016/S1359-6454(98)00031-7.

[6] A. Ejlali, A. Ejlali, K. Hooman, H. Gurgenci, Application of high porosity metal foams as air-cooled heat exchangers to high heat load removal systems, Int. Commun. Heat Mass Transf. 36 (7) (2009) 674–679, http://dx.doi.org/10.1016/j.icheatmasstransfer.2009.03.001.

[7] J. Fernández, R. Poulter, Radial mass flow in electrohydrodynamically-enhanced forced heat transfer in tubes, Int. J. Heat Mass Transf. 30 (10) (1987) 2125–2136, http://dx.doi.org/10.1016/0017-9310(87)90091-3.

[8] M.K. Bologa, I.K. Savin, A.B. Didkovsky, Electric-field-induced enhancement of vapour condensation heat transfer in the presence of a non-condensable gas, Int. J. Heat Mass Transf. 30 (8) (1987) 1577–1585, http://dx.doi.org/10.1016/0017-9310(87)90302-4.

[9] J.W. Zhou, Y.G. Wang, G. Middelberg, H. Herwig, Unsteady jet impingement: heat transfer on smooth and non-smooth surfaces, Int. Commun. Heat Mass Transf. 36 (2) (2009) 103–110, http://dx.doi.org/10.1016/j.icheatmasstransfer.2008.10.020.

[10] P. Xu, B. Yu, S. Qiu, H.J. Poh, A.S. Mujumdar, Turbulent impinging jet heat transfer enhancement due to intermittent pulsation, Int. J. Therm. Sci. 49 (7) (2010) 1247–1252, http://dx.doi.org/10.1016/j.ijthermalsci.2010.01.020.

[11] S. Iijima, Helical microtubules of graphitic carbon, Nature 354 (6348) (1991) 56–58, http://dx.doi.org/10.1038/354056a0.

[12] M.-S. Liu, M. Ching-Cheng Lin, I.T. Huang, C.-C. Wang, Enhancement of

thermal conductivity with carbon nanotube for nanofluids, Int. Commun. Heat Mass Transf. 32 (9) (2005) 1202–1210, http://dx.doi.org/10.1016/j.icheatmasstransfer.2005.05.005.

[13] K.-J. Park, D. Jung, Enhancement of nucleate boiling heat transfer using carbon nanotubes, Int. J. Heat Mass Transf. 50 (21–22) (2007) 4499–4502, http://dx.doi.org/10.1016/j.ijheatmasstransfer.2007.03.012.

[14] S. Launay, A.G. Fedorov, Y. Joshi, A. Cao, P.M. Ajayan, Hybrid micro-nano structured thermal interfaces for pool boiling heat transfer enhancement, Microelectron. J. 37 (11) (2006) 1158–1164, http://dx.doi.org/10.1016/j.mejo.2005.07.016.

[15] Z.-H. Liu, L. Liao, Forced convective flow and heat transfer characteristics of aqueous drag-reducing fluid with carbon nanotubes added, Int. J. Therm. Sci. 49 (12) (2010) 2331–2338, http://dx.doi.org/10.1016/j.ijthermalsci.2010.08.001.

[16] P. Kim, L. Shi, A. Majumdar, P.L. Mceuen, Thermal transport measurements of individual multiwalled nanotubes, Phys. Rev. Lett. 87 (21) (2001) 215502.

[17] S. Sinha, S. Barjami, G. Iannacchione, A. Schwab, G. Muench, Off-axis thermal properties of carbon nanotube films, J. Nanoparticle Res. 7 (6) (2005) 651–657, http://dx.doi.org/10.1007/s11051-005-8382-9.

[18] H. Xie, A. Cai, X. Wang, Thermal diffusivity and conductivity of multiwalled carbon nanotube arrays, Phys. Lett. A 369 (1–2) (2007) 120–123, http://dx.doi.org/10.1016/j.physleta.2007.02.079.

[19] I. Tuzovskaya, S. Pacheco Benito, J.K. Chinthaginjala, C. Reed, L. Lefferts, T. Van Der Meer, Heat exchange performance of stainless steel and carbon foams modified with carbon nano fibers, Int. J. Heat Mass Transf. 55 (21–22) (2012) 5769–5776, http://dx.doi.org/10.1016/j.ijheatmasstransfer.2012.05.073.

[20] K. Kordás, G. Tóth, P. Moilanen, M. Kumpumäki, J. Vähäkangas, A. Uusimäki, R. Vajtai, P.M. Ajayan, Chip cooling with integrated carbon nanotube microfin architectures, Appl. Phys. Lett. 90 (12) (2007), http://dx.doi.org/10.1063/1.2714281.

[21] Z. Mo, R. Morjan, J. Anderson, E.E.B. Campbell, L. Johan, in: Integrated Nanotube Microcooler for Microelectronics Applications vol. 1, 2005, pp. 51–54, http://dx.doi.org/10.1109/ECTC.2005.1441244.

[22] T.J. Taha, L. Lefferts, T.H. Van Der Meer, Indirect involvement of amorphous carbon layer on convective heat transfer enhancement using carbon nanofibers, J. Heat Transf. 137 (9) (2015), http://dx.doi.org/10.1115/1.4030218, 091007–091007.

[23] T.J. Taha, D.B. Thakur, T.H.V.D. Meer, Towards convective heat transfer enhancement: surface modification, characterization and measurement techniques, J. Phys. Conf. Ser. 395 (1) (2012) 012113, http://dx.doi.org/10.1088/1742-6596/395/1/012113.

[24] R.J. Moffat, Describing the uncertainties in experimental results, Exp. Therm. Fluid Sci. 1 (1) (1988) 3–17, http://dx.doi.org/10.1016/0894-1777(88)90043-X.

[25] A.N. Karwa, V.A. Davis, B.J. Tatarchuk, Carbon nanofiber synthesis within 3-Dimensional sintered nickel microfibrous matrices: optimization of synthesis conditions, J. Nanotechnol. 2012 (2012) 14, http://dx.doi.org/10.1155/2012/396269.

[26] P. Liu, L. Lefferts, Preparation of carbon nano-fiber washcoat on porous silica foam as structured catalyst support, Chin. J. Chem. Eng. 14 (3) (2006) 294–300, http://dx.doi.org/10.1016/S1004-9541(06)60074-8.

[27] D.B. Thakur, R.M. Tiggelaar, J.G.E. Gardeniers, L. Lefferts, K. Seshan, Silicon based microreactors for catalytic reduction in aqueous phase: use of carbon nanofiber supported palladium catalyst, Chem. Eng. J. 227 (2013) 128–136, http://dx.doi.org/10.1016/j.cej.2012.08.067.

[28] J. Yu, Y. Tian, X. Ma, Y. Li, Studies in Surface Science and Catalysis, Elsevier, A New Composite Micro/Meso Porous Material Used as the Support of Catalyst for Polyaromatic Compound Hydrogenation, 2010.

[29] F. Li, L. Lefferts, T.H. Meer Van Der, Study on Heat Transfer Enhancement by Metallic Foams with Carbon Nano Fibers (CNFs), in: 6th World Conference on Experimental Heat Transfer, Fluid Mechanics, and Thermodynamics, (Matsushima, Miyagi, Japan), 2005, pp. 17–21.

[30] S. Lee, K. Cheng, V. Palmre, M.D.M.H. Bhuiya, K.J. Kim, B.J. Zhang, H. Yoon, Heat transfer measurement during dropwise condensation using micro/nano-scale porous surface, Int. J. Heat Mass Transf. 65 (2013) 619–626, http://dx.doi.org/10.1016/j.ijheatmasstransfer.2013.06.016.

[31] N.D. Ngo, K.K. Tamma, Microscale permeability predictions of porous fibrous media, Int. J. Heat Mass Transf. 44 (16) (2001) 3135–3145, http://dx.doi.org/10.1016/S0017-9310(00)00335-5.

[32] S. Ergun, Fluid flow through packed columns, Chem. Eng. Progr. 48 (2) (1952) 89–94.

[33] F. Fachin, G.D. Chen, M. Toner, B.L. Wardle, Integration of bulk nanoporous elements in microfluidic devices with application to biomedical diagnostics, Microelectromech. Syst. J. 20 (6) (2011) 1428–1438, http://dx.doi.org/10.1109/JMEMS.2011.2167669.

[34] V. Lysenko, J. Vitiello, B. Remaki, D. Barbier, Gas permeability of porous silicon nanostructures, Phys. Rev. E 70 (1) (2004) 017301.

[35] J. Maultzsch, S. Reich, C. Thomsen, E. Dobardžić, I. Milošević, M. Damnjanović, Phonon dispersion of carbon nanotubes, Solid State Commun. 121 (9–10) (2002) 471–474, http://dx.doi.org/10.1016/S0038-1098(02)00025-X.

[36] H. Ishii, N. Kobayashi, K. Hirose, Electron–phonon coupling effect on quantum transport in carbon nanotubes using time-dependent wave-packet approach, Phys. E Low-dimens. Syst. Nanostruct. 40 (2) (2007) 249–252, http://dx.doi.org/10.1016/j.physe.2007.06.006.

[37] A. Kasuya, Y. Saito, Y. Sasaki, M. Fukushima, T. Maedaa, C. Horie, Y. Nishina, Size dependent characteristics of single Wall carbon nanotubes, Mater. Sci. Eng. A 217–218 (1996) 46–47, http://dx.doi.org/10.1016/S0921-5093(96)10357-9.

[38] T. Maeda, C. Horie, Phonon modes in Single-Wall nanotubes with a small diameter, Phys. B Condens. Matter 263–264 (1999) 479–481, http://dx.doi.org/10.1016/S0921-4526(98)01415-X.

[39] P.G. Klemens, D.F. Pedraza, Thermal conductivity of graphite in the basal plane, Carbon 32 (4) (1994) 735–741, http://dx.doi.org/10.1016/0008-6223(94)90096-5.

[40] D.F. Pedraza, P.G. Klemens, Effective conductivity of polycrystalline graphite, Carbon 31 (6) (1993) 951–956, http://dx.doi.org/10.1016/0008-6223(93)90197-I.

[41] F. Tuinstra, J.L. Koenig, Raman spectrum of graphite, J. Chem. Phys. 53 (3) (1970) 1126–1130, http://dx.doi.org/10.1063/1.1674108.

[42] M.A. Pimenta, G. Dresselhaus, M.S. Dresselhaus, L.G. Cancado, A. Jorio, R. Saito, Studying disorder in graphite-based systems by Raman spectroscopy, Phys. Chem. Chem. Phys. 9 (11) (2007) 1276–1290, http://dx.doi.org/10.1039/B613962K.

[43] P. Lespade, R. Al-Jishi, M.S. Dresselhaus, Model for Raman scattering from incompletely graphitized carbons, Carbon 20 (5) (1982) 427–431, http://dx.doi.org/10.1016/0008-6223(82)90043-4.

[44] P. Lespade, A. Marchand, M. Couzi, F. Cruege, Caracterisation De Materiaux Carbones Par Microspectrometrie Raman, Carbon 22 (4–5) (1984) 375–385, http://dx.doi.org/10.1016/0008-6223(84)90009-5.

[45] M. Endo, K. Nishimura, Y.A. Kim, K. Hakamada, T. Matushita, M.S. Dresselhaus, G. Dresselhaus, Raman spectroscopic characterization of submicron vapor-grown carbon fibers and carbon nanofibers obtained by pyrolyzing hydrocarbons, J. Mater. Res. 14 (12) (1999) 4474–4477, http://dx.doi.org/10.1557/JMR.1999.0607.

[46] C. Kim, S.-H. Park, J.-I. Cho, D.-Y. Lee, T.-J. Park, W.-J. Lee, K.-S. Yang, Raman spectroscopic evaluation of polyacrylonitrile-based carbon nanofibers prepared by electrospinning, J. Raman Spectrosc. 35 (11) (2004) 928–933, http://dx.doi.org/10.1002/jrs.1233.

[47] A. Aitkaliyeva, M.S. Martin, T.A. Harriman, D.S. Hildebrand, D.A. Lucca, J. Wang, D. Chen, L. Shao, Radiation effects on the D to G Raman intensities of carbon nanotubes, Phys. Rev. B 89 (23) (2014) 235437.

[48] Y. Miyata, K. Mizuno, H. Kataura, Purity and defect characterization of single-wall carbon nanotubes using Raman spectroscopy, J. Nanomater. 2011 (2011) 7, http://dx.doi.org/10.1155/2011/786763.

[49] L.G. Cançado, K. Takai, T. Enoki, M. Endo, Y.A. Kim, H. Mizusaki, A. Jorio, L.N. Coelho, R. Magalhães-Paniago, M.A. Pimenta, General equation for the determination of the crystallite size La of nanographite by Raman spectroscopy, Appl. Phys. Lett. 88 (16) (2006), http://dx.doi.org/10.1063/1.2196057.

[50] R. Taylor, The thermal conductivity of pyrolytic graphite, Philos. Mag. 13 (121) (1966) 157–166, http://dx.doi.org/10.1080/14786436608211993.

[51] M.G. Holland, C.A. Klein, W.D. Straub, The Lorenz number of graphite at very low temperatures, J. Phys. Chem. Solids 27 (5) (1966) 903–906, http://dx.doi.org/10.1016/0022-3697(66)90265-4.

[52] J.K. Chinthaginjala, D.B. Thakur, K. Seshan, L. Lefferts, How carbon-nano-fibers attach to Ni foam, Carbon 46 (13) (2008) 1638–1647, http://dx.doi.org/10.1016/j.carbon.2008.07.002.